RESEARCH ARTICLE

Design of an Additively-Manufactured Self-Supported All-Metal Coaxial-Line X-Band Bandpass Filter

ALEJANDRO PONS-ABENZA[1,2], **IVAN ARREGUI**[2], **(Member, IEEE)**,
MIGUEL ANGEL GOMEZ LASO[2], **(Fellow, IEEE)**, **TXEMA LOPETEGI**[2], **(Member, IEEE)**,
AND PETRONILO MARTIN-IGLESIAS[2,3], **(Senior Member, IEEE)**

[1]Department of Information and Communication Technologies, Technical University of Cartagena (UPCT), Cartagena, 30202 Murcia, Spain
[2]Department of Electrical, Electronic, and Communications Engineering, Institute of Smart Cities (ISC), Public University of Navarre (UPNA), Campus Arrosadia, 31006 Pamplona, Spain
[3]European Space Agency (ESA), 2201 AZ Noordwijk, The Netherlands

Corresponding author: Alejandro Pons-Abenza (alejandro.pons@upct.es)

ABSTRACT In this contribution, the design and manufacturing of an all-metal coaxial-line X-band bandpass filter is discussed. The device is 3D-printed as a self-supported structure without any dielectric inside the coaxial. The mechanical support between the inner and outer coaxial-line conductors is provided by means of $\lambda/4$ short-circuited stubs, which are also used in the bandpass filter design. The real transmission zeros (TZs) produced by the short-circuited stubs are responsible for a high filter selectivity. In order to enhance the filter performance, a second stage consisting in a coaxial-line stepped-impedance low-pass filter is integrated in the design to provide the rejection level required for the out-of-band behaviour. Following our design method, the bandpass and low-pass filters are designed separately, and a final matching step is performed to connect both and to achieve the aimed frequency specifications. In this way, a monoblock coaxial filter with very good in-band and out-of-band performance can by obtained by using an additive manufacturing (AM) procedure. Only the input/output (I/O) coaxial connectors will need to be assembled to the filter to perform the frequency measurements. The filters in this work can be seen as a first proposal towards more complex multi-functional monoblock structures using additively-manufactured coaxial technology, for highly-integrated RF chains. Other expected benefits beyond the compactness or lightweight are an increased RF shielding, electrostatic discharge risk reduction, and Passive Intermodulation (PIM) protection. In the paper, a prototype with a passband between 8 and 12 GHz is designed and manufactured, using a bandpass filter with three stubs and an integrated 15th-order low-pass filter, providing rejection for spurious frequencies up to 30 GHz. The filter is manufactured using Selective Laser Melting (SLM) and measurements show an excellent agreement with the simulations.

INDEX TERMS Bandpass filter, coaxial-line filter, metal 3D-printing, stepped-impedance filter.

I. INTRODUCTION

Coaxial technology has dominated RF design in low-frequency bands, both for high- and low- power applications. It provides clear advantages in terms of compactness, which

The associate editor coordinating the review of this manuscript and approving it for publication was Kai-Da Xu.

gives rise to a potential for highly integrated RF modules. However, simultaneously increasing the RF system's complexity and compactness poses significant challenges for conventional manufacturing techniques such as milling and turning. These challenges grow exponentially with the frequency of operation. While ad-hoc processes, such as PolyStrata [1], [2], [3] have emerged as potential end-to-end manufacturing solutions for high-frequency coaxial-based RF systems, their widespread adoption remains limited.

In the latest few years, additive manufacturing has emerged as a potential technology for radio-frequency (RF) and microwave devices. One of the major challenges in the current state-of-the-art in 3D-printing applied to RF devices lies in the manufacturing of coaxial-based transmission lines [4]. Traditionally, coaxial-line structures have been manufactured by milling the enclosure and placing the internal conductor with its dielectric into the structure [5]. The dielectric part allows to sustain the inner conductor along the coaxial line axis. It also reduces the transmission line dimensions, but at the cost of additional ohmic losses. Moreover, the conventional manufacturing approach of combining metal and dielectric components, while cost-effective, imposes limitations on the geometries that can be realized, leading to a situation where the manufacturing process dictates the RF design.

This paper presents a novel approach to achieve complex RF functionality by combining a low-pass filter, which provides a wide rejection band, with a bandpass filter that enhances rejection near the transmission band. This initial step towards multi-functional RF structures introduces the challenge of increased complexity in manufacturing and assembly. The manufacturing as a monoblock structures using coaxial technology without any dielectric inside the device is expected to offer additional benefits beyond compactness or lightweight, such as increased RF shielding, reduced electrostatic discharge risk between inner and outer coaxial part, and a higher threshold for Passive Intermodulation (PIM). The elimination of dielectric supports necessitates the implementation of structural components to support the inner conductor within the outer coaxial section. These structural elements should not compromise the compactness of the design, and it is desirable to incorporate them as active components that influence the overall transfer function. An extensive literature review was conducted to identify existing dual-purpose RF topologies that simultaneously serve as both structural and filtering elements.

We should clarify that, within the filter literature, this work is focused on the study and design of coaxial-line structures. Unlike the well-known coaxial resonator-based filters, our structures are based on coaxial lines with a pure TEM mode.

On the contrary, coaxial resonators are typically used to develop compact resonant cavities, using TM modes [6], [7]. In this sense, there exist many designs in the technical literature where coaxial resonator cavities are employed [8],

but not so many filter designs relying on coaxial-line structures can be found.

Using 3D-printing, it is possible to manufacture a coaxial-line I/O section to implement the coupling with a cavity resonator built in a different technology, as it was done in [9] making use of a waveguide resonator. A more complex example can be found in [10], where the authors propose a $\lambda_g/2$-coaxial-line resonator design using a meandered topology for the filter. In this case, a hybrid manufacturing is proposed: the inner conductor of the coaxial line is 3D-printed using a stereolithography technique (SLA) in a polymer, which is then metallized and soldered to a rectangular waveguide housing that behaves as the coaxial-line outer conductor.

In [11], a complete 4-port magic-Tee is proposed, which includes a coaxial-to-waveguide transition using also self-supported coaxial-lines, but without any further practical electrical functionality in the design. Moreover, this piece was manufactured using a SLA procedure, and several holes were required to ensure a proper metallization of the inner faces. This solution can be troublesome for satellite applications, for instance, due to the different thermal expansion coefficients of metals and dielectrics. Another interesting structure using coaxial-lines is presented in [12]. In this case, a self-supported coaxial-line is designed and manufactured using two short-circuited stubs. The part was manufactured by a selective laser melting (SLM) technique, using a copper alloy. This approach eliminates the requirement of a posterior metallization of the inner surfaces of the structure. The mechanical support provided by the parallel stub presented in [12] restricts the bandwidth where the coaxial-line can be used, but the device is not exploited as a filter and no clear guidelines for a filter design are given. Indeed, its practical usefulness as a filter is limited, for instance, by its out-of-band behaviour. Moreover, several holes for dumping the residual dust were also required, which also becomes a problem, for instance, in a space application.

To demonstrate the dual-purpose topology, structural supporting and filtering, a coaxial-line bandpass filter using aluminium 3D-printing is proposed in this work, giving also clear design guidelines. The section responsible for the bandpass functionality is the most suitable candidate for the dual-purpose function, while the low-pass section was selected to follow a more conventional topology. The objective is to build a monoblock part for a satellite filter, with a bandpass at X-band (from 8 to 12 GHz), and with a wide spurious free range up to 30 GHz. The filtering function to accomplish the required specifications is achieved by integrating a bandpass filter of parallel short-circuited stubs with a low-pass stepped-impedance filter. The parallel stub filter is designed to be in charge of the passband and, simultaneously, provide the physical support between the inner and outer coaxial conductors, whereas the low-pass section rejects the spurious resonances of the bandpass filter up to 30 GHz, as required by the specifications. The

bandpass filter topology was selected to demonstrate enough self-supporting capability of the overall structure with the minimum number of structural supports. The low number of structural supports will also serve to verify the stability of the block during manufacturing and assembly. This will result in a 3-pole only bandpass transfer function, which can be further enhanced in potential practical applications needing sharper responses (more filter poles), to achieve improved selectivity within the passband.

Both stages (bandpass and low-pass filters) are designed separately, as it will be discussed in Section II. The final structure consists in a monoblock filtering device obtained by cascading the bandpass filter with the stepped-impedance low-pass filter. To account for the loading effects between the two filters, the first coaxial-line sections of the low-pass filter can be modified to match the required return loss (RL) level of the resulting filter if needed.

The final proposed device is manufactured using a SLM procedure with a suitable aluminium alloy (AlSi10Mg). The piece can be cleaned very easily and, in particular, no holes for dumping the dust are needed. As it is demonstrated in section III, the obtained results show an excellent agreement with the simulations up to high frequencies in the out-of-band, thus validating the approach presented in the paper. This is expected to be very useful for other monoblock coaxial-line 3D-printed devices.

II. DESIGN OF THE COAXIAL-LINE FILTER

In this section, the design strategy for the proposed 3D-printed self-supported coaxial-line filter structure is discussed. The first stage is a bandpass filter designed as a parallel short-circuited stub structure, and its aim is to implement a passband in the intended frequency range (8 to 12 GHz, in our example). In addition, the short-circuits provided by the stubs give the mechanical design required for a self-supported all-metal coaxial-line structure. The second stage is a stepped-impedance coaxial-line low-pass filter, which is in charge of enhancing the spurious performance of the first stage, removing the spurious resonances up to 30 GHz in our example. Once the two filters are designed, the two parts are connected through a coaxial line, and the physical dimensions of the initial coaxial-line sections in the low-pass filter are modified to account for the loading effects produced by the cascaded connection between the bandpass and low-pass filters.

In a typical coaxial-line, the characteristic impedance Z_0 of the fundamental TEM mode is analytical, and its numerical value can be calculated as [13]

$$Z_0 = \sqrt{\frac{\mu}{\varepsilon}} \frac{\ln(D/d)}{2\pi}, \qquad (1)$$

where d is the inner conductor diameter, D is the outer conductor diameter, and $\varepsilon = \varepsilon_0 \varepsilon_r$ is the dielectric permittivity of the material filling the coaxial line. For the designs presented in this paper, $\varepsilon_r = 1$, as the coaxial lines will be always filled with air. Moreover, the external conductor
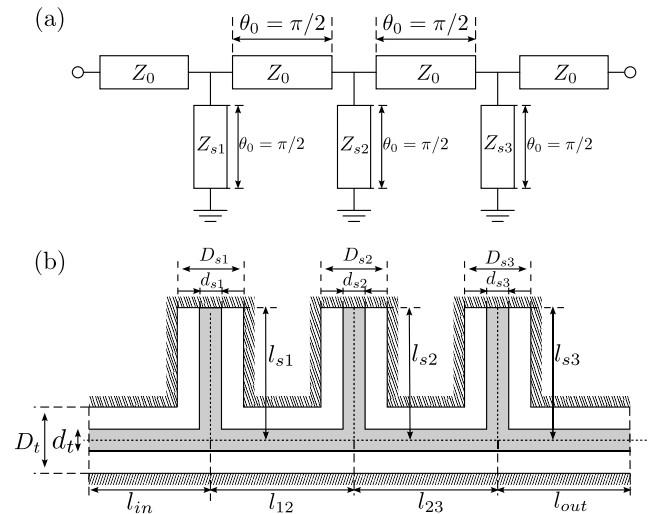

FIGURE 1. 2D sketch of the proposed parallel short-circuited stub bandpass filter. (a) Ideal transmission line model with $\lambda_0/4$ lines at the filter central frequency f_0, where θ_0 is the electrical length of the transmission line at f_0, Z_0 is the characteristic impedance at the ports, and Z_{s1}, Z_{s2}, and Z_{s3} are the characteristic impedances of each stub obtained through direct synthesis. (b) 2D parametrization of the coaxial short-circuited stub model, where D_t and d_t are the outer and inner conductor diameters of the main line in the structure, respectively. D_{s1}, D_{s2}, and D_{s3} are the outer conductor diameters of the parallel stubs, whereas d_{s1}, d_{s2}, and d_{s3} are their inner conductor diameters.

diameter is kept constant, whereas the inner conductor diameter is modified to obtain the required impedance value. This simplifies the design of the final prototype. The outer diameter is chosen, for each of the designed filters, according to manufacturing or electrical constraints, which are properly detailed in its corresponding Section below.

A. PARALLEL STUB BANDPASS FILTER

The bandpass filter is designed using a parallel short-circuited stub approach. This allows implementing the filter and, additionally, it benefits from the mechanical support provided by the short circuits at each stub end. Physically, the short-circuit is done in the coaxial-line stubs by electrically connecting the coaxial inner and outer conductors. This is very useful to achieve an all-metal coaxial-line structure, and it is exploited to allow the monoblock manufacturing of the whole filtering device. A 2D sketch of the proposed parallel short-circuited stub filter, using 3 stubs, is depicted in Fig. 1(b).

For the sake of simplicity, the inner and outer conductor diameters of the main line of the bandpass filter (BPF) are constant (d_t and D_t, respectively), as well as the stubs outer conductor diameter D_{si}. The stubs inner conductor diameters d_{si} will be used to obtain the required stub impedances Z_{si}. Considering the characteristic impedance of the coaxial connector ($Z_{conn} = 50\ \Omega$) that will be attached at the BPF input, the dimensions of D_t and d_t need to be chosen accordingly. It is important to observe that, for a fixed value of the coaxial-line characteristic impedance, a small value of D_t means an even smaller value of d_t, which may

result in a geometry impossible to achieve by means of 3D-printing. Taking into account the SLM manufacturing process, a minimum of 1-mm thickness is recommended to avoid mechanical problems during the 3D-printing process, such as thermal stress on the inner conductor. For this reason, a value of $D_t = 5$ mm is selected, which results in a value of $d_t = 2.16$ mm, doubling the minimum recommended size, for a coaxial-line $Z_t = 50\ \Omega$. It should be also remarked that larger values of D_t will reduce the cut-off frequency of the higher-order modes in the coaxial-line structure. However, a poor spurious performance in the BPF is not critical, as long as no spurious resonances interfere with the filter passband. The frequency rejection in the out-of-band between 12 GHz and 30 GHz will be addressed using the low-pass filter (LPF) described in Section II-B.

In principle, the filter might be synthesized using the coupling-matrix formalism, considering the short-circuit stubs as resonators (whose length and impedance can be adjusted to tune their resonant frequency) and the coaxial lines connecting the stubs as inter-resonator couplings (again, the length and impedance is adjusted to obtain the required coupling level). However, this is a classical filter topology that can be accurately and more simply designed through well-known analytical equations [14], which is the approach followed here. The BPF synthesis consists in extracting the characteristic impedances of the parallel stubs (Z_{s1}, Z_{s2} and Z_{s3}) and the transmission lines connecting them (Z_{12} and Z_{23}), given that all transmission lines have an electrical length of $\lambda_0/4$, where λ_0 is the wavelength corresponding to the filter central frequency f_0. Expressions for these characteristic impedances can be found in [14] as a function of the filter frequency specifications (central frequency, bandwidth and in-band return loss). However, this classical approach can not be replicated in our design because of the restriction imposed for $Z_{12} = Z_{23} = Z_{\mathrm{conn}}$. In [13], a convenient simplification is deduced from the classical design equations that consider a fixed characteristic impedance for the transmission lines Z_{12} and Z_{23}, following the philosophy of our proposed BPF. The ideal transmission line equivalent circuit corresponding to this example is presented in Fig. 1(a). The expression for each short-circuited parallel stub impedance Z_{si} is then evaluated as

$$Z_{si} = \frac{\pi Z_0 \Delta}{4 g_i}, \qquad (2)$$

where Z_0 is the characteristic impedance of the ports (Z_{conn}), $\Delta = \mathrm{BW}/f_0$ is the filter fractional bandwidth, and g_i is the corresponding element extracted from a Chebyshev low-pass prototype synthesis. In this design, the low-pass prototype elements for a Chebyshev response can be computed considering the filter order ($N = 3$), with return loss $RL = 30$ dB, resulting in $g_0 = g_4 = 1$, $g_1 = g_3 = 0.5358$, and $g_2 = 0.8817$. The characteristic impedances for each stub are then evaluated as $Z_{s1} = Z_{s3} = 29.32\ \Omega$, and $Z_{s2} = 17.81\ \Omega$. In the coaxial-line model, the outer conductor diameters D_{s1}, D_{s2} and D_{s3} are fixed to 4 mm, and the inner conductor
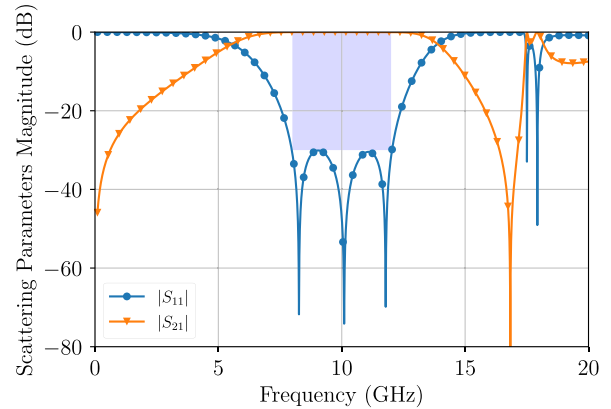

FIGURE 2. Scattering parameter response of the parallel stub filter, corresponding to the schematic shown in Fig. 3, simulated with CST MWS. The shadowed rectangle indicates the $|S_{11}|$ goal employed during the filter optimization.

TABLE 1. Physical dimensions of the parallel stub filter, comparing the initial values obtained through the synthesis and the final optimized values, following the parametrization shown in Fig. 3. The external diameter of the coaxial stubs is fixed to $D_{s1} = D_{s2} = D_{s3} = 4$ mm. Due to input-output symmetry, $l_{s3} = l_{s1}$, $l_{23} = l_{12}$ and $d_{s3} = d_{s1}$. All dimensions are given in mm.

Model	d_{s1}	d_{s2}	l_{s1}	l_{s2}	l_{12}
Initial	2.45	2.97	7.5	7.5	7.5
Optimized	1.56	2.01	9.63	9.33	7.69

diameters are calculated to achieve the required parallel stub impedances using (1), resulting in $d_{s1} = d_{s3} = 2.45$ mm, and $d_{s2} = 2.97$ mm. However, even though the ideal transmission line model provides a good starting point, there exist some electromagnetic effects which are not considered in this equivalent circuit. Therefore, an optimization step with the full-wave simulator CST Microwave Studio (CST MWS) is required. The optimization is performed considering the stubs impedances $Z_{s1} = Z_{s3}$ and Z_{s2} through the coaxial stubs inner conductors $d_{s1} = d_{s3}$ and d_{s2}. Also, the physical length of the coaxial lines $l_{12} = l_{23}$ is taken into account. An optimization goal to fit $|S_{11}|$ under -30 dB, imposing the condition over the range between the passband (8 GHz and 12 GHz), is enough to obtain the required frequency response. This happens because the scattering parameter response simulated with the physical dimensions calculated through the transmission line model results in a response that is close enough to the filter required frequency specifications. The final optimized response obtained after the optimization procedure is shown in Fig. 2, validating the design strategy proposed for the BPF with short-circuited stubs. For the sake of completeness, the initial and optimized values corresponding to this design are collected in Table 1.

While the design described in the previous paragraph could be used in the complete monoblock filtering device, the parallel stubs connected orthogonally to the main coaxial-line of the filter pose a significant challenge in terms of practical feasibility. In order to avoid the introduction of additional supports during the 3D-printing process, the stubs are carefully reoriented in the BPF to allow a support-less
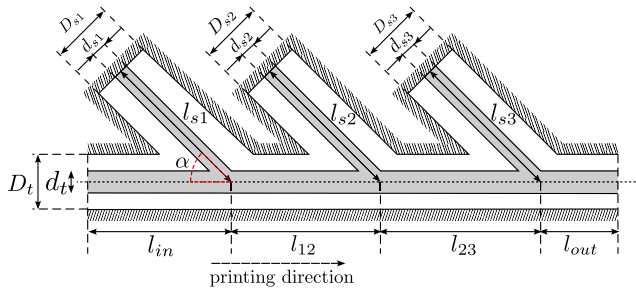
FIGURE 3. 2D sketch illustrating the parametrization of the stub-based transition allowing the self-supported manufacturing of the proposed device. D_t and d_t are the external and internal conductor diameters of the main line in the structure, respectively. D_{s1}, D_{s2}, and D_{s3} are the external conductor diameters of the parallel stubs, whereas d_{s1}, d_{s2}, and d_{s3} are the internal conductor diameters.

TABLE 2. Physical dimensions of the optimized parallel stub filter, following the parametrization shown in Fig. 3. The external diameter of the coaxial stubs is fixed to $D_{s1} = D_{s2} = D_{s3} = 4$ mm. All dimensions are given in mm.

Parameter	Value	Parameter	Value
d_t	2.16	l_{s2}	8.996
D_t	5	l_{s3}	7.77
d_{s1}	1.65	l_{in}	5
d_{s2}	2.035	l_{12}	7.567
d_{s3}	1.485	l_{23}	7.754
l_{s1}	9.293	l_{out}	3

fabrication. Specifically, the stubs are rotated with an angle of $\alpha = 45°$ with respect to the printing direction, as indicated in Fig. 3.

The new proposed geometry requires an additional optimization step, although the BPF response is close to the frequency requirements, and thus, only the final dimensions from this process are collected in Table 2. It is important to remark that, after the stubs are rotated from its original position, the filter loses its input to output symmetry, and thus, the interconnection lengths l_{12} and l_{23}, the stub lengths l_{s1} and l_{s3}, and the stub inner diameters d_{s1} and d_{s3} will no longer be equal. This issue must be considered during the final optimization stage to accomplish the frequency specifications for the filter response. The final response of the optimized BPF with rotated parallel stubs is presented in Fig. 4.

As a final note regarding the BPF design incorporating parallel stubs, it's worth emphasizing that augmenting the number of stubs in the filter can amplify its frequency selectivity. Moreover, each additional parallel stub introduces an extra transmission zero (TZ) within the rejection band, potentially bolstering frequency selectivity in the upper out-of-band response. Nevertheless, these additional TZs lack independent control since their frequency positioning hinges on the stub length, a crucial parameter in BPF design. While this aspect offers a notable benefit of the proposed structure, it cannot be directly harnessed during the design phase.

B. LOW-PASS STEPPED-IMPEDANCE COAXIAL-LINE FILTER

The low-pass coaxial-line filter is designed as a commensurate-line stepped-impedance structure. A 2D
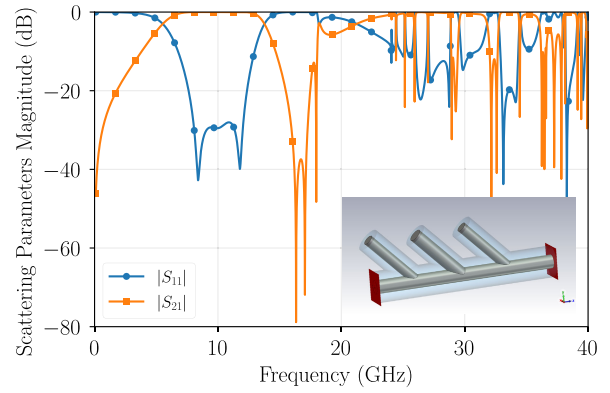

FIGURE 4. Scattering parameter response of the final optimized bandpass filter with short-circuited parallel stubs, corresponding to dimensions depicted in table 2. In the inset, a 3D model of the designed BPF is shown, as modeled in the full-wave software CST MWS.

sketch of the proposed filter is illustrated in Fig. 5. This structure consists in a cascade of $N + 2$ coaxial-line sections with the same outer conductor diameter, D, and different inner conductor diameters, d_i. The proposed design method begins with the computation of the normalized characteristic impedances $Z_i(norm)$ of the commensurate-line distributed unit element prototype, providing the desired all-pole filtering response [15]. To obtain the normalized impedances, a Chebyshev response is taking into account the filter order ($N = 15$), return loss level ($RL = 30$ dB), the low-pass cut-off frequency ($f_c = 12$ GHz), and the frequency where the maximum $|S_{21}|$ rejection is achieved ($f_r = 24$ GHz). The filter order, N, is obtained to ensure a minimum $|S_{21}|$ level of -75 dB at f_r, and can be computed as a function of this requirement, the frequencies f_r and f_c, and the RL level (in dB), as [16]

$$N = \frac{\cosh^{-1}\left(\sqrt{\left(\frac{1}{|S_{21}|^2_{min}} - 1\right) \cdot \left(10^{\frac{RL}{10}} - 1\right)}\right)}{\text{sech}^{-1}\left(\cos\left(\frac{\pi}{2} \cdot \frac{f_r - f_c}{f_r}\right)\right)}. \quad (3)$$

Evaluating (3), the required filter order is 14.5 in our case. However, since N has to be an integer, it is fixed to $N = 15$. An odd filter order allows the first and last sections of the low-pass filter to have the same characteristic impedance, simplifying the filter design. In our example, the computed normalized impedances are $Z_1 = Z_{17} = 1$, $Z_2 = Z_{16} = 1.2751$, $Z_3 = Z_{15} = 0.6516$, $Z_4 = Z_{14} = 1.9630$, $Z_5 = Z_{13} = 0.4931$, $Z_6 = Z_{12} = 2.2609$, $Z_7 = Z_{11} = 0.4611$, $Z_8 = Z_{10} = 2.3333$, and $Z_9 = 0.4552$. Thanks to the fact that the commensurate-line model that is employed in the low-pass filter synthesis relies on the cascading of ideal transmission lines with electrical length θ_c at the low-pass cut-off frequency f_c [15], the physical dimensioning of the coaxial-line filter is straightforward, as a pure TEM mode propagation is supported by the coaxial. First, the normalized impedances $Z_i(norm)$ are scaled with the reference impedance of the ports: $Z_i(scaled) = 50 \, \Omega \cdot$
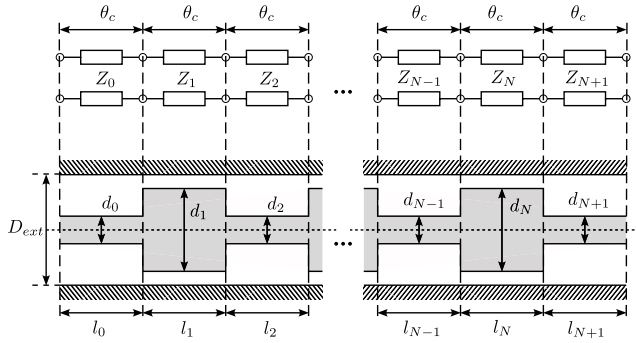
FIGURE 5. 2D sketch illustrating the correspondence between the transmission line SI model of the low-pass filter and the physical dimensions of the physical coaxial-line filter, where θ_c is the transmission line electrical length at the low-pass cut-off frequency f_c, Z_0, Z_1,..., Z_{N+1} are the synthesized characteristic impedances for the transmission line sections, d_0, d_1,...,d_{N+1} are the inner conductor diameters corresponding to the synthesized impedances and l_0, l_1,...,l_{N+1} are their corresponding physical lengths. D_{ext} is the outer conductor diameter, which is constant for all the coaxial-line sections. Only the initial and final steps of the filter are shown.
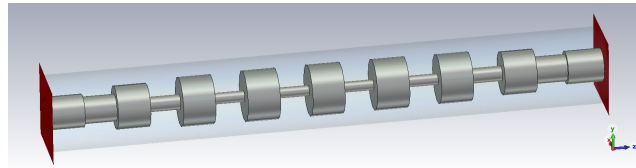

FIGURE 7. Frequency responses of several low-pass coaxial-line filters designed with different external conductor diameters. For the sake of clarity, only the $|S_{21}|$ (dB) is shown in the plot. The curve labelled as "Tx-line model" corresponds to the $|S_{21}|$ (dB) response of the commensurate-line distributed unit element prototype, included as a reference for comparison purposes.

FIGURE 6. 3D view of the standard coaxial-line low-pass filter, as designed in the full-wave software CST MWS.

$Z_i(norm)$. Then, the inner conductor diameter d_i is computed for each coaxial section, according to the scaled impedance computed from the synthesis, following (1), with a fixed outer diameter D and $\varepsilon_r = 1$. The physical length of each section is determined by θ_c, which can be calculated from f_c and f_r as

$$\theta_c = \frac{\pi}{2} \cdot \frac{f_c}{f_r}, \qquad (4)$$

resulting in $\theta_c = 45°$ in our designed LPF. It should be remarked that (4) is valid only for ideal transmission line implementations (like our coaxial-line case) [17].

The next step is to choose a suitable outer conductor diameter D_i. Similarly as it was discussed in Section II-A, the outer conductor diameter D_i will be kept constant for each section of the LPF filter. However, because the low-pass filter is built using a stepped-impedance (SI) approach, the geometry is composed by coaxial-line sections whose characteristic impedance will be higher and lower than the reference port impedance of 50 Ω. Typically, the synthesis of these SI low-pass responses results in alternating high- and low-impedance transmission lines, which is translated into coaxial inner conductor diameters alternating between small and large values, as it is observed in Fig. 6.

At this point, there exist two major issues that need to be addressed. The first one is related to the manufacturing constraints of the 3D-printing process. As it is discussed in Section II-A, the minimum size for the inner conductor
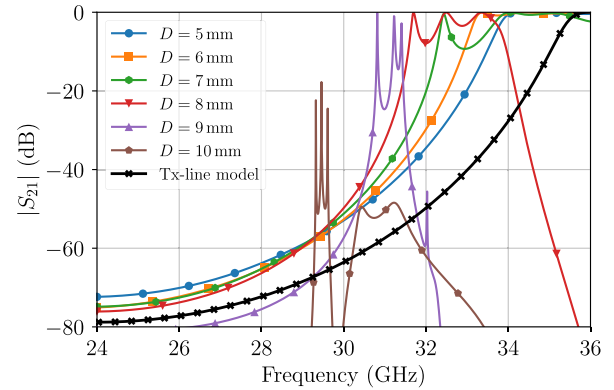
diameter should be 1 mm. During the SI LPF design, the coaxial-line sections with the highest impedance will show very thin inner conductor diameters, which must be avoided. The second issue is related with the LPF spurious performance. Assuming a pure TEM single-mode operation, and considering the specifications described at the beginning of this section, the stepped-impedance commensurate-line distributed prototype (shown in Fig. 5) will exhibit a spurious-free range of $2(f_r - f_c) = 24$ GHz, i.e., the first replica begins at $2f_r - f_c = 36$ GHz, see [17]. However, even though the coaxial-line operates with a TEM mode, spurious effects can be observed when the outer conductor diameter is increased, since the spurious excitation of higher order modes is also enhanced. This higher-order mode excitation is more noticeable as the frequency increases, reducing the width of the LPF rejected band.

To evaluate these issues, several filter examples with different values of the outer conductor diameter have been simulated, all designed following the procedure described at the beginning of this Section. A total of six low-pass filters are compared, with outer diameter D fixed to values ranging from 5 mm to 10 mm. The design parameters are the inner conductor diameters and the lengths corresponding to each section, as illustrated in Fig. 5. For each filter, their frequency specifications are the same, and as those given above. The frequency responses of each filter are presented in Fig. 7, where only the magnitude of the S_{21} parameter is plotted, for the sake of clarity. The frequency span ranges from 24 GHz to 36 GHz, in order to properly observe the transmission response at higher frequencies too.

As expected, the influence of the higher-order mode excitation on the frequency response of the designed coaxial-line filters is more noticeable as the outer conductor diameter D is increased. This effect results in a spurious-free range reduction of the designed coaxial-line filters, as compared to the reference $|S_{21}|$ curve corresponding to the commensurate-line distributed unit element prototype, where a pure TEM

TABLE 3. Physical dimensions of several low-pass coaxial-line filters designed with different outer conductor diameters. Diameters and lengths given range from sections 0 to 8. Sections 9 to 16 are symmetrical ($d_9 = d_7$, $d_{10} = d_6$, …). Dimensions are given in mm.

D	d_0	d_1	d_2	d_3	d_4	d_5	d_6	d_7	d_8	l_1	l_2	l_3	l_4	l_5	l_6	l_7	l_8
5	2.16	1.87	2.8	0.916	3.25	0.73	3.32	0.66	3.34	2.98	2.77	2.67	2.59	2.81	2.66	2.75	2.66
6	2.61	2.26	3.22	1.18	3.86	0.84	3.98	0.88	4.1	0.78	2.03	2.54	2.29	2.67	2.47	2.86	2.27
7	3.04	2.42	4.06	1.36	4.64	1.06	4.77	1	4.79	0.22	1.25	2.59	1.88	2.89	1.92	2.96	1.91
8	3.47	2.76	4.65	1.56	5.3	1.21	5.45	1.14	5.45	1.22	1.50	2.69	1.70	2.87	1.7	2.94	1.66
9	3.91	3.11	5.23	1.75	5.97	1.37	6.13	1.29	6.16	3.10	2.99	2.82	2.68	2.63	2.60	2.59	2.58
10	4.34	4.65	4.84	2.37	6.10	2.05	6.31	1.56	6.31	3.03	2.76	2.33	2.46	3.13	2.50	2.59	2.58

single-mode operation is ensured. In fact, it is easy to observe that larger D values produce spurious transmission peaks at lower frequencies. In this sense, it would be better to employ the lowest D value possible. However, inspecting the resulting inner conductor diameters (collected in Table 3), these are very thin for the smallest D designs. To avoid problems during the 3D-printing process, we will fix a minimum of 1 mm thickness in the smallest inner conductor diameter. Thus, the filter with $D = 8$ mm is chosen for manufacturing, as its minimum inner diameter is 1.14 mm, which corresponds to d_7, and the first spurious frequency is located beyond 30 GHz.

In order to obtain an accurate dimensional synthesis of the coaxial low-pass filter, the fringing fields produced due to the inner conductor discontinuities must be considered, as they introduce an electromagnetic effect that is not present in the ideal equivalent circuit. To account for this effect in the design procedure, a physical length refinement can be applied. As it is discussed in [14], the compensation required will be different for each impedance step, as it will strongly depend on the diameter difference between the two sections considered in the discontinuity. For this reason, the physical length of each i−th section will not be equal for all the LPF sections.

Let us consider the discontinuity between section i and $i + 1$, where the ports are placed at an electrical distance of $\theta_c/2$. Because the physical length of each section should be ideally equal to $l_c = 3.125$ mm (the physical length corresponding to θ_c at the cutoff frequency, 12 GHz), it is possible to define the length of each coaxial section l_i as a function of the fixed l_c physical length, and the compensation length from the fringing field analysis $\Delta l_{i,i+1}$ as

$$l_i = l_c - \Delta l_{(i-1,i)} - \Delta l_{(i,i+1)}, \quad (5)$$

where $\Delta l_{(i-1,i)}$ is the compensation length between sections $i - 1$ and i. In practice, the compensation length $\Delta l_{(i,i+1)}$ for a discontinuity between sections i and $i + 1$, can be obtained through the parametric analysis of the geometry illustrated in Fig. 8. For each section in the discontinuity, a half electrical length $\theta_c/2$ line is considered, as the target value for the analysis. The physical length of this $\theta_c/2$ coaxial-line is now defined as

$$l_{test} = l_c/2 - \Delta l_{(i,i+1)}, \quad (6)$$

where l_c is the theoretical physical length that corresponds to a θ_c electrical length, and $\Delta l_{(i,i+1)}$ is the compensation
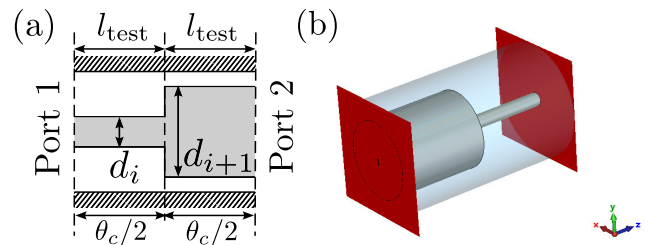

FIGURE 8. Illustration of the coaxial-line impedance step employed to compensate the effect due to the fringing fields. (a) 2D sketch of the impedance step showing the relevant physical parameters employed in the refinement procedure. (b) 3D model as designed with CST Studio Suite 2022 for the EM simulation adjustment.
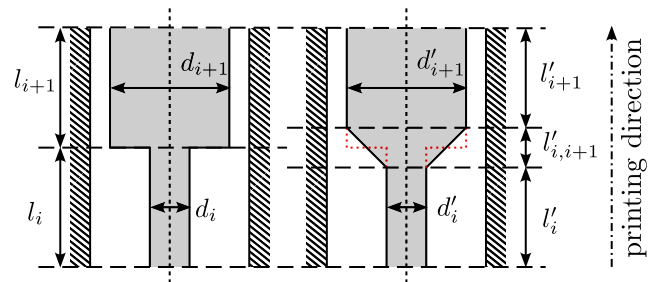

FIGURE 9. 2D sketch illustrating the modification introduced to allow a support-less manufacturing of the inner conductor. The standard impedance step is shown in the left coaxial section, while the proposed modification to the steps is illustrated in the right section. The length of the cone section is fixed to $d'_{i+1} - d'_i$ to ensure a 45° growing angle for the 3D printing.

length due to the fringing fields effect described in the previous paragraph. In a practical case, the section with each coaxial step discontinuity shown in Fig. 8(a) is physically dimensioned by adjusting the S_{21} phase. By design, $\angle S_{21}$ should be equal to $-\theta_c$ at the filter cutoff frequency $f_c = 12$ GHz. This process must be repeated throughout all the coaxial step discontinuities in the filter, and the adjusted l_i lengths are calculated using (5).

Finally, the structure still needs to be adapted to allow the layer-by-layer manufacturing process of the metal 3D-printing. The solution proposed in this paper is to place the filter in the growing direction of the 3D-printing machine. In this case, it is easy to observe, from Fig. 5, that building the inner conductor from a large radius to a smaller one is simple, but the opposite leaves the following section overhanging. This situation is depicted in Fig. 9, where the standard impedance step is indicated with the red dotted lines.
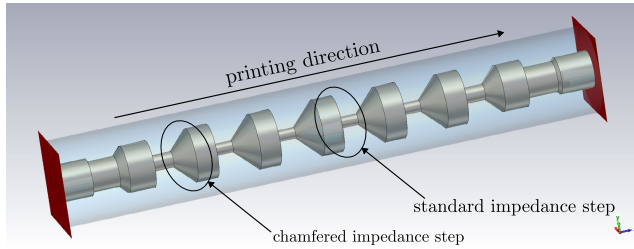
FIGURE 10. 3D model of the designed low-pass coaxial-line filter, as modeled in the full-wave software CST. The filter integrates standard impedance steps and chamfered impedance steps, depending on the constraints to allow a 3D printing, as described in Fig. 9.

FIGURE 11. Frequency response of the coaxial-line low-pass filter, after being modified as described in Fig. 9.

FIGURE 12. Illustration of the final device designed for 3D printing. A transversal cut-plane is presented, to reveal the inner part of the coaxial structure. Flanges for a SMA coaxial-line connector are included in the I/O ports.

To solve this, it is possible to introduce a gradual (chamfered) impedance step to avoid hanging parts during the 3D-printing process. This modification allows a supportless fabrication of the inner conductor. However, the filter physical dimensions need to be slightly tuned accordingly.

A 2D-sketch of the proposed modification is depicted in Fig. 9 for the i-th impedance step. The introduction of this chamfered section is characterized by its length and slope. Due to the layer-by-layer manufacturing process, the minimal angle of growth of the solid with respect to the printing direction should be 45°. To achieve this angle of growth in the structure, we can model the chamfered section as a truncated cone, whose bottom diameter is d_i', its top diameter is d_{i+1}', and its height is the length $l_{i,i+1}' = d_{i+1}' - d_i'$.

In order to reproduce the frequency response of the standard low-pass filter section after introducing the chamfered impedance steps, an adjustment in the coaxial internal conductor diameter and its length is required. In this work, this procedure was performed by applying a matching technique. First, the reflection coefficient of the standard coaxial-line section, using the diameters d_i and d_{i+1}, is simulated, and its S_{21} magnitude is used as a target to obtain the diameters of the coaxial-line section with the chamfered impedance step of diameters d_i' and d_{i+1}'. After these diameters are obtained, using CST for instance, the S_{21}-phase of the standard section can be used to match the phase of the chamfered impedance-step section, obtaining the proper values of the section lengths l_i' and l_{i+1}'. This procedure is repeated for each impedance step whose geometry cannot be 3D printed due to the inner conductor diameter overhanging. The sections that can be kept unaltered and the ones that are modified can be clearly identified in the 3D-model view shown in Fig. 10. As it can be seen in the figure, only the steps where a small radius changes into a large radius are modified, introducing the described truncated cone to avoid the overhanging.

It is important to remark that, in the procedure presented in this work, the LPF geometry is initially designed through the synthesis of the standard model without chamfered impedance steps. Of course, if the geometry adaptation to a 3D-printing process is not needed, the design procedure would stop at the fringing field compensation step described in Fig. 8.
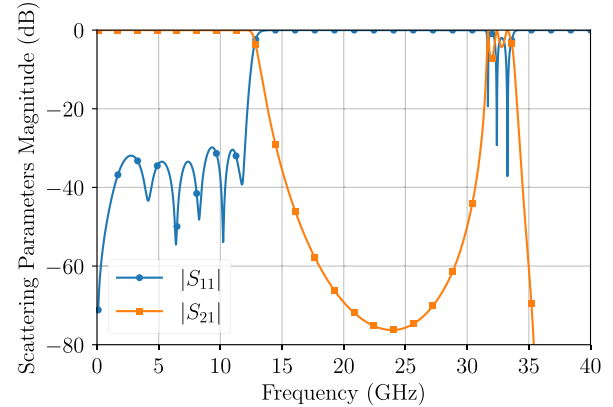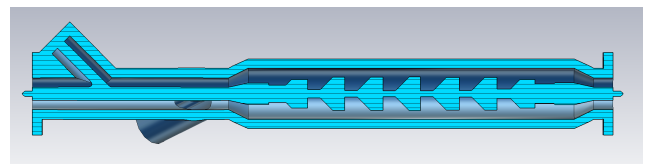
After applying the design procedure described above, the frequency response of the filter is presented in Fig. 11. As expected, a perfect return loss equalization is achieved, and a clean out-of-band appears up to around 30 GHz.

C. CONNECTING THE BPF AND THE LPF
After the bandpass and low-pass filters have been designed, the electrical response when we put them together must be considered before manufacturing. The reflection from both filters are properly equalized inside the filter passband between 8 and 12 GHz, but some out-of-band degradation is expected after cascading, due to the resonant interactions between the two filters. A 3-D view of the resulting monoblock filter is depicted in Fig. 12.

There are some features added to the 3D-model in Fig. 12 which were not considered during the design stage. First, the flanges for a wall-mounted SMA-type coaxial connector are included at the input and output ports of the device. At the low-pass filter output port, a geometrical adaptation from an outer conductor diameter of 8 mm to 5 mm is incorporated, while keeping a constant output impedance of 50 Ω. A similar geometrical feature is added at the low-pass filter input port, which helps to connect the bandpass stub filter (whose outer conductor diameter is 5 mm) and the stepped-impedance filter (with an outer conductor diameter of 8 mm). This 50-Ω to 50-Ω coaxial transition is designed to be easily manufactured in the 3D-printer, following a similar strategy as that shown in Section II-B to avoid overhanging of the cylindrical parts. In the low-pass filter output port, this
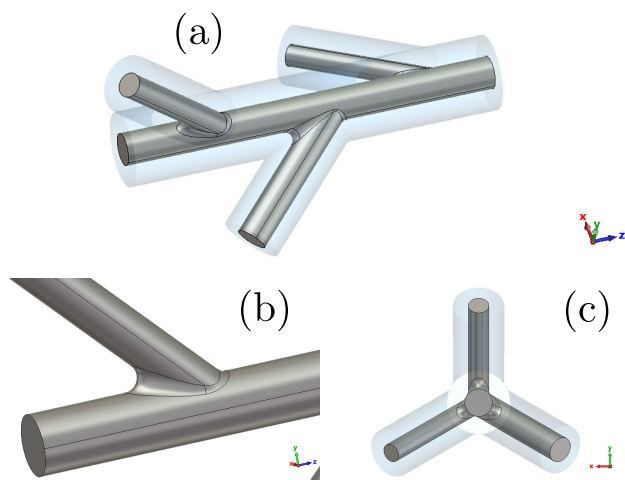
FIGURE 13. Some CAD model views of the stubs filter to be manufactured after connecting to the low-pass filter. (a) 3D view of the piece. (b) Detail of the rounded edges connecting a stub and the coaxial main line. (c) Bottom view to illustrate the stub distribution along the XY plane.

FIGURE 14. S-Parameter response of the final optimized device.

FIGURE 15. Photograph illustrating some manufactured prototypes without the coaxial connectors attached, showing the flange details at the connection face.

transition is not strictly required, because the inner conductor diameter goes from a larger to a lower value, which can be handled by the 3D-printer. However, a small gap would appear due to the inner conductor of the filter being too close to the outer conductor at the port (5 mm and 3.47 mm, respectively). To avoid future high-power handling issues, the transition was also included here. It should be remarked that this transition has very little effect on the whole filter electrical response.

In addition, the parallel stub filter layout is re-oriented to produce an optimized geometry for 3D-printing. As it is observed in Fig. 12, the three stubs are rotated with respect to the main inner conductor of the filter. In fact, the position of each stub in the coaxial transversal plane has been rotated 120° with respect to each other. The objective is to provide a better mechanical support to the whole device once the piece starts to be printed. Because the support points are evenly distributed around the coaxial line, it is expected that errors due to misalignment or inclination of the piece are minimized. Moreover, the sharp edges at the coaxial inner conductor joints of the main line and stubs are rounded, in order to avoid thermal stress on those edges during the building process. A detailed view of the stub filter with these features incorporated is shown in Fig. 13.

The frequency response of the whole device is depicted in Fig. 14 for a frequency span from 0 to 40 GHz (dashed lines). It can be observed that the reflection level $|S_{11}|$ is below -25 dB within the passband, and the first spurious band is still beyond 30 GHz, showing a similar behaviour as the isolated low-pass filter in the stop-band. However, there exist some peak resonances close to the passband around 13-14 GHz. These appear due to the standing wave generated between the last stub of the bandpass filter and the first impedance step of the low-pass section. This electromagnetic effect is typical when cascading a low-pass and a bandpass filter,
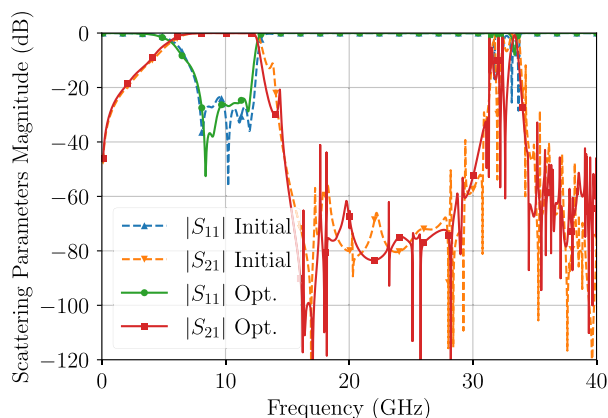
although it is possible to minimize its impact on the device performance by modifying the length of this connection, while keeping a good equalization within the passband and a large spurious-free range, as required by the application. The final electrical response of the device after these adjustments are implemented is shown in Fig. 14 with continuous lines.

III. MEASUREMENTS AND MANUFACTURING
The optimized design whose frequency response is shown in Fig. 14 is now manufactured using SLM. Thanks to the introduction of the bandpass stub filter, the inner and outer conductors in the coaxial structure are self-supported. For this manufacturing, a ReniShaw RenAM 500 3D-printer is employed. The printing material is a well-known aluminium alloy (AlSi10Mg), whose electrical conductivity values typically range between $1.7986 \cdot 10^7$ S/m and $2.3474 \cdot 10^7$ S/m [18]. The 3D-printing process is performed inside an argon atmosphere. The expected dimensional tolerance is $\pm 100 \ \mu m$, and the layer thickness of the 3D-printer is fixed to 60 μm. No post-printing treatment is applied to the built part, and only a mechanical polishing is applied to the external faces of the I/O flanges, ensuring an adequate flatness before assembling the SMA connectors to
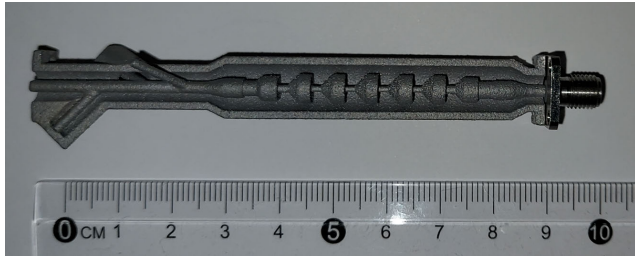
FIGURE 16. Photograph of a filter sample printed without half of the outer conductor cylinder, to enable visual inspection of the device inner surfaces, with an SMA coaxial connector attached to the filter output port.
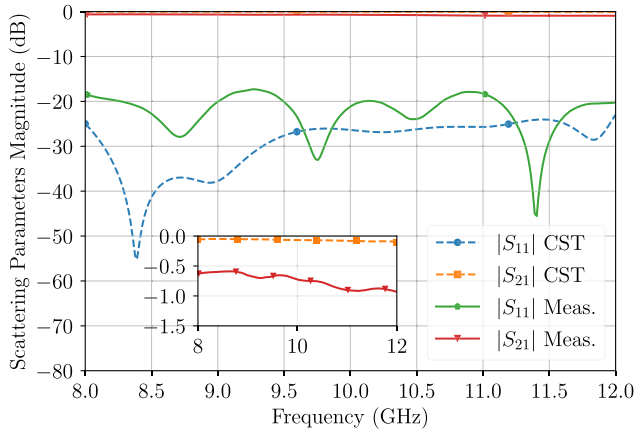

FIGURE 17. S-parameter response of the measured prototype, as compared to the full-wave simulation with lossy walls for the 3D piece. In the inset, a graph comparing the simulated and measured $|S_{21}|$ (dB) levels is presented.

FIGURE 18. S-parameter response of the measured prototype, as compared to the full-wave simulation with lossy walls for the 3D piece. The frequency span is enlarged in this measurement, validating the frequency rejection up to 30 GHz.

the 3D-printed part. In Fig. 15, a photograph showing three manufactured prototypes are presented. In these prototypes, it can be clearly observed the I/O pin that is 3D-printed and the surface around it that is manually polished to connect with a wall-mounted female coaxial connector. In addition, one of the devices was cut to visually inspect the filter inner details, and a photograph is shown in Fig. 16.

First, a measurement of the passband scattering parameters corresponding to one of the prototypes is performed. The measurements are performed with an Agilent E8364B PNA vector network analyzer. The results are compared to the simulations in Fig. 17. The measured bandwidth and cut-off frequency show an excellent agreement with the simulated response. It is worth noting that the measured $|S_{11}|$ equalization is slightly worse than in simulation. This is due to the dimensional tolerance of the 3D-printing. Still, the measured return loss is never smaller than 18 dB, which is very good. The measured insertion loss (IL) is 0.722 dB at the filter central frequency, while a value equal to 0.066 dB is obtained in simulation when considering an electrical conductivity of $6.2 \cdot 10^6$ S/m, a value reported in similar fabrications with AlSi10Mg [17]. There exist two factors that contribute to the observed increase in the filter IL. The main contribution comes from the surface roughness in the inner walls of the filter, which is not considered in the full-wave
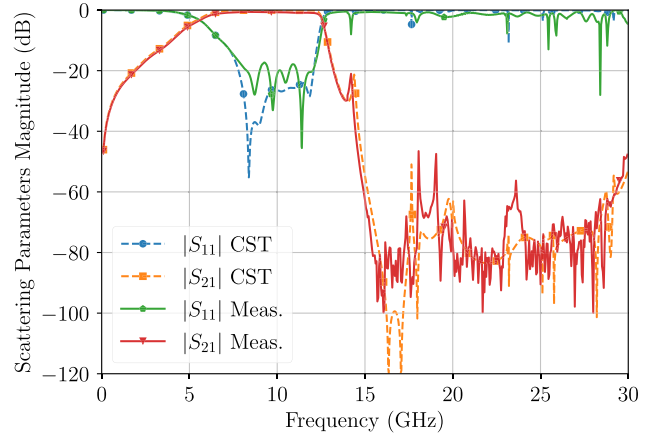
simulations. In addition, the worse matching of the $|S_{11}|$ parameter can also contribute to measure a lower $|S_{21}|$ value. It is also possible that a significant contribution to the overall filter loss comes from a non-optimal connection between the wall-mounted SMA connector and the 3D-printed part interface, since this effect is not taken either into account in the full-wave simulation. In summary, the measurements of the manufactured prototype in the passband are very satisfactory, thus validating the design strategy proposed in this work.

A second measurement is carried out enlarging the frequency span of the PNA after performing a new calibration. The objective is to validate the wide spurious-free range up to 30 GHz. The results from this measurement are compared to the full-wave simulation in Fig. 18. As calibrations in Fig. 17 and Fig. 18 are not the same, there are some minor discrepancies between them until 14 GHz. This is not relevant and it should be highlighted that a wide spurious-free range is obtained, with a $|S_{21}|$ level below -50 dB, between 15 and 30 GHz. Again, the measured S-parameters show an excellent agreement with the simulations also in the out-of-band.

For the sake of completeness, an additional comparison between the proposed monoblock filter and other devices from the technical literature is presented in Table 4. Our filter is compared with transitions (which may also exhibit an intrinsic filtering performance), low-pass, and bandpass filters operating at similar frequency bands and considering various technologies. The proposed coaxial-line monoblock filter represents an excellent trade-off between bulkier technologies with remarkable loss performance, such as the waveguide, and more compact technologies with poor rejection bands, such as SIW and other planar technologies. To the authors' knowledge, the presented filter is the first all-metal monoblock microwave filter in coaxial-line technology, and it represents a significant step towards the development of highly-integrated microwave chains for satellite applications.

TABLE 4. Comparison to other filters and devices with intrinsic filtering performance published in the literature. SIW: Substrate Integrated Waveguide. QMSIW: Quarter-Mode SIW. ESICL: Empty Substrate Integrated Coaxial Line. SLM: Selective Laser Melting. SLA: Stereolithography. CNC: Computerized Numerical Control. PCB: Printed Circuit Board. N/A: Not Applicable. N/G: Not Given.

Reference	Type	Technology	Operation range	Rejection	Manufacturing Technology	Monoblock
[12]	Transition	Coaxial-line	12 to 26 GHz	N/G	SLM (Copper)	Yes
[11]	Transition	Coaxial-line	8 to 13 GHz	N/G	SLA + metallization	Yes
[19]	Low-pass filter	Waveguide	10.7 to 12.7 GHz	Up to 40 GHz	CNC Milling	No
[20]	Low-pass filter	Waveguide	10.7 to 12.7 GHz	Up to 40 GHz	Electroforming	Yes
[17]	Low-pass filter	Waveguide	10.7 to 11.7 GHz	Up to 22 GHz	SLM (AlSi10Mg)	Yes
[5]	Low-pass filter	Coaxial-line	DC to 6 GHz	Up to 14 GHz	CNC Milling + dielectric	No
[21]	Bandpass filter	SIW	9.5 to 10 GHz	Up to 17 GHz	PCB	N/A
[22]	Bandpass filter	QMSIW	8.1 to 9.3 GHz	Up to 17.5 GHz	PCB	N/A
[23]	Bandpass filter	ESICL	2.97 to 3.03 GHz	N/G	PCB	N/A
[24]	Bandpass filter	Waveguide	14 to 14.5 GHz	Up to 33 GHz	CNC Milling	No
[10]	Bandpass filter	Coaxial-line	2.975 to 3.025 GHz	Up to 6 GHz	Hybrid (SLA + CNC Milling)	No
[25]	Bandpass filter	Waveguide	14 to 14.25 GHz	Up to 33 GHz	SLM (Scalmalloy)	Yes
[26]	Bandpass filter	Waveguide	9.85 to 10.15 GHz	Up to 13 GHz	SLA + metallization	Yes
This work	Bandpass filter	Coaxial-line	8 to 12 GHz	Up to 30 GHz	SLM (AlSi10Mg)	Yes

IV. CONCLUSION

In this work, a monoblock coaxial-line filter is designed, manufactured and tested. The combination of a bandpass filter to fulfill the required frequency specifications in the passband and a low-pass filter to effectively reject higher spurious frequencies is commonly employed in satellite communication payloads. Our approach involves designing and fabricating both components of the RF chain together, using a 3D-printed all-metal self-supported coaxial-line. The prototype developed and presented in this contribution has exhibited excellent behaviour and agreement with the full-wave simulations, even with only three supporting stubs (bandpass filter poles), thereby validating the feasibility of the proposed approach towards a highly integrated monoblock coaxial-line filter. Consequently, the proposed design paves the way to intricate multi-functional monoblock structures in coaxial-line technology, leading to coaxial RF chains that benefit from compactness, RF shielding, and electrostatic discharge-risk and PIM reduction.

ACKNOWLEDGMENT

REFERENCES

[1] J.-M. Rollin, D. Miller, M. Urteaga, Z. M. Griffith, and H. Kazemi, "A PolyStrata® 820 mW G-band solid state power amplifier," in *Proc. IEEE Compound Semiconductor Integr. Circuit Symp. (CSICS)*, Oct. 2015, pp. 1–4.

[2] J. W. Jordan, W. Stacy, J. Ng, B. L. Cannon, A. Caba, K. J. Vanhille, J. Clough, B. Stant, and P. E. Racette, "PolyStrata® X/Ku/K/Ka-band, dual-polarized, tightly coupled dipole scannable focal plane array," in *Proc. IEEE Int. Symp. Antennas Propag. USNC/URSI Nat. Radio Sci. Meeting*, Jul. 2018, pp. 817–818.

[3] E. Wagner, T. LaRocca, M. Verderber, C. Rezende, and P. May, "A 31-tap reconfigurable analog FIR filter using heterogeneously integrated polystrata delay-lines," *IEEE Microw. Wireless Compon. Lett.*, vol. 32, no. 6, pp. 648–651, Jun. 2022.

[4] P. Martín-Iglesias, M. Marechal, P. Calves, M. Hazard, L. Pambaguian, A. Brandao, S. Rodriguez Castillo, T. Martin, J. Percaz, V. Iza, S. Martín-Iglesias, I. Arregui, F. Teberio, T. Lopetegi, and M. A. G. Laso, "Metal 3D printing for RF/microwave high-frequency parts," *CEAS Space J.*, vol. 15, no. 1, pp. 7–25, Jan. 2023.

[5] E. YiLMAZ and M. Üçüncü, "Coaxial low-pass filter design and manufacture," *IEEE Access*, vol. 11, pp. 15845–15854, 2023.

[6] D. Sh-Asanjan and R. R. Mansour, "A novel coaxial resonator for high power applications," in *Proc. 44th Eur. Microw. Conf.*, Oct. 2014, pp. 295–298.

[7] K. Zhao and D. Psychogiou, "Monolithic multiband coaxial resonator-based bandpass filter using stereolithography apparatus (SLA) manufacturing," *IEEE Trans. Microw. Theory Techn.*, vol. 70, no. 9, pp. 4156–4166, Sep. 2022.

[8] K. Zhao and D. Psychogiou, "Monolithically-integrated 3D printed coaxial bandpass filters and RF diplexers: Single-band and dual-band," *Int. J. Microw. Wireless Technol.*, vol. 14, no. 3, pp. 293–304, Apr. 2022.

[9] J. Cazden, L. Boskovic, E. Lier, T. Hand, W. N. Kefauver, and D. Filipovic, "Performance of SLA and DMLS 3D printed Ka-band resonators with integrated coaxial launchers," in *Proc. 51st Eur. Microw. Conf. (EuMC)*, Apr. 2022, pp. 338–341.

[10] G. Venanzoni, M. Dionigi, C. Tomassoni, and R. Sorrentino, "Design of a compact 3D printed coaxial filter," in *Proc. 48th Eur. Microw. Conf. (EuMC)*, Sep. 2018, pp. 280–283.

[11] C. Guo, J. Li, Y. Yu, F. Zhang, Y. Zhu, Q. Yang, W. Zhu, S. Zhu, X. Shang, Y. Gao, Y. Wang, G.-L. Huang, Q. S. Cheng, and A. Zhang, "A 3-D printed *E*-plane waveguide magic-T using air-filled coax-to-waveguide transitions," *IEEE Trans. Microw. Theory Techn.*, vol. 67, no. 12, pp. 4984–4994, Dec. 2019.

[12] L. Boskovic, J. Cazden, and D. Filipovic, "Design and characterization of an all-metal 3-D printed air-dielectric coaxial line," *IEEE Microw. Wireless Compon. Lett.*, vol. 32, no. 7, pp. 839–842, Jul. 2022.

[13] D. M. Pozar, *Microwave Engineering*, 4th ed. Hoboken, NJ, USA: Wiley, 2012.

[14] G. Matthaei, L. Young, and E. Jones, *Microwave Filters, Impedance-matching Networks, and Coupling Structures* (Artech House Microwave Library). Norwood, MA, USA: Artech House, 1980. [Online]. Available: https://books.google.es/books?id=cRMoAQAAMAAJ

[15] R. J. Cameron, C. M. Kudsia, and R. R. Mansour, *Microwave Filters for Communication Systems: Fundamentals, Design and Applications*. Hoboken, NJ, USA: Wiley, Mar. 2018.

[16] I. Arnedo, M. Chudzik, J. M. Percaz, I. Arregui, F. Teberio, D. Benito, T. Lopetegi, and M. A. G. Laso, "Synthesis of one dimensional electromagnetic bandgap structures with fully controlled parameters," *IEEE Trans. Microw. Theory Techn.*, vol. 65, no. 9, pp. 3123–3134, Sep. 2017.

[17] J. M. Percaz, J. Hussain, I. Arregui, F. Teberio, D. Benito, P. Martin-Iglesias, I. Arnedo, M. A. G. Laso, and T. Lopetegi, "Synthesis of rectangular waveguide filters with smooth profile oriented to direct metal additive manufacturing," *IEEE Trans. Microw. Theory Techn.*, vol. 71, no. 7, pp. 3081–3101, Jul. 2023.

[18] R. R. J. Sélo, S. Catchpole-Smith, I. Maskery, I. Ashcroft, and C. Tuck, "On the thermal conductivity of AlSi10Mg and lattice structures made by laser powder bed fusion," *Additive Manuf.*, vol. 34, Aug. 2020, Art. no. 101214. [Online]. Available: https://www.sciencedirect.com/science/article/pii/S2214860420305868

[19] I. Arregui, F. Teberio, I. Arnedo, A. Lujambio, M. Chudzik, D. Benito, R. Jost, F. J. Gortz, T. Lopetegi, and M. A. G. Laso, "High-power low-pass harmonic waveguide filter with te_{n0}-mode suppression," *IEEE Microw. Wireless Compon. Lett.*, vol. 22, no. 7, pp. 339–341, Jul. 2012.

[20] I. Arregui, F. Teberio, I. Arnedo, A. Lujambio, M. Chudzik, D. Benito, T. Lopetegi, R. Jost, F.-J. Gortz, J. Gil, C. Vicente, B. Gimeno, V. E. Boria, D. Raboso, and M. A. G. Laso, "High-power low-pass harmonic filters with higher-order te_{n0} and non-te_{n0} mode suppression: Design method and multipactor characterization," *IEEE Trans. Microw. Theory Techn.*, vol. 61, no. 12, pp. 4376–4386, Dec. 2013.

[21] J. D. Martinez, S. Sirci, M. Taroncher, and V. E. Boria, "Compact CPW-fed combline filter in substrate integrated waveguide technology," *IEEE Microw. Wireless Compon. Lett.*, vol. 22, no. 1, pp. 7–9, Jan. 2012.

[22] Z. He, C. J. You, S. Leng, X. Li, and Y.-M. Huang, "Compact bandpass filter with high selectivity using quarter-mode substrate integrated waveguide and coplanar waveguide," *IEEE Microw. Wireless Compon. Lett.*, vol. 27, no. 9, pp. 809–811, Sep. 2017.

[23] L. Martinez, A. Belenguer, V. E. Boria, and A. L. Borja, "Compact folded bandpass filter in empty substrate integrated coaxial line at S-band," *IEEE Microw. Wireless Compon. Lett.*, vol. 29, no. 5, pp. 315–317, May 2019.

[24] P. Vallerotonda, L. Pelliccia, C. Tomassoni, F. Cacciamani, R. Sorrentino, J. Galdeano, and C. Ernst, "Compact waveguide bandpass filters for broadband space applications in C and Ku-bands," in *Proc. Eur. Microw. Conf. Central Eur. (EuMCE)*, May 2019, pp. 116–119.

[25] P. Booth and E. V. Lluch, "Enhancing the performance of waveguide filters using additive manufacturing," *Proc. IEEE*, vol. 105, no. 4, pp. 613–619, Apr. 2017.

[26] C. Guo, X. Shang, J. Li, F. Zhang, M. J. Lancaster, and J. Xu, "A lightweight 3-D printed X-band bandpass filter based on spherical dual-mode resonators," *IEEE Microw. Wireless Compon. Lett.*, vol. 26, no. 8, pp. 568–570, Aug. 2016.

IVAN ARREGUI (Member, IEEE) received the Telecommunication Engineering, M.Sc., and Ph.D. degrees from the Public University of Navarre (UPNA), Pamplona, Spain, in 2005, 2008, and 2013, respectively.

He is currently an Assistant Professor with the Electrical, Electronic and Communications Engineering Department, UPNA. He is the Co-Founder of TAFCO Metawireless S.L., a spin-off company of UPNA. His current research interests include periodic structure devices for microwave, millimeterwave and terahertz frequency ranges, numerical techniques for the inverse scattering synthesis, and the design of passive components for communications satellites. He received a grant from the Spanish Ministry of Science and Innovation and several prizes, including the Extraordinary Doctorate Prize of UPNA, the HISDESAT Prize from the Spanish Telecommunications Engineers Association (COIT/AEIT) for the Best Doctoral Dissertation in Satellite Services, and the Innovation Award from Alberto Elzaburu Foundation.

MIGUEL ANGEL GOMEZ LASO (Fellow, IEEE) received the M.Sc. and Ph.D. degrees in telecommunications engineering from the Public University of Navarre (UPNA), Pamplona, Spain, in 1997 and 2002, respectively. From 1998 to 2001, he was a Doctoral Fellow Student with the Electrical and Electronic Engineering Department, UPNA, where he was an Assistant Professor, from 2001 to 2006. From 2002 to 2003, he was a Research Fellow with the Payload Systems Division, European Space Research and Technology Centre, European Space Agency (ESTEC-ESA), Noordwijk, The Netherlands. He is currently the Head of the Microwave Components Group (MCG), UPNA. He is the Co-Founder of TAFCO Metawireless S.L., a spin-off company of UPNA. He has been an Associate Professor (Professor Titular), since 2006, always involved in teaching and research duties related to optical communications and microwave engineering. He has led projects with public and private funding within MCG and UPNA. He has authored or coauthored dozens of journal articles and contributed to major international conferences. He holds several international patents. His research interests include periodic structures, inverse scattering problems, synthesis techniques for filters and multiplexers in the microwave and millimeter-wave frequency ranges, and their applications in wireless and space communications. He is a member of several professional and scientific international associations, including the Optical Society of America (OSA), the International Society for Optics and Photonics (SPIE), and the American Society for Engineering Education (ASEE). He is also a member of MTT-5 Filters and the MTT-S Education Committee. He is a TPRC Member of the MTT-S International Microwave Symposium (IMS) and a reviewer for several other international conferences and journals. He received several prizes, including the Spanish National Prize to the Best Doctoral Dissertation in Telecommunications from the Spanish Telecommunications Engineers Association (COIT/AEIT), in 2002; the Junior Research Award of UPNA, in 2003; and the 2005 Spanish National Prize for the Best Project in Innovation in Higher Education from the Spanish Ministry of Education and Science. He is the current President of the URSI Spanish National Committee. He was the Co-Chair of the EuMC'18 (Madrid) and the Education Resources Development Subcommittee. He is the Chair of the Working Group of Standards for Microwave Filter Definitions, IEEE Standards Committee. He was an Associate Editor of IEEE Transactions on Microwave Theory and Techniques, from 2019 and 2022.

ALEJANDRO PONS-ABENZA was born in Murcia, Spain, in 1990. He received the master's degree in telecommunications systems engineering and the Ph.D. degree in communications and information technology from the Technical University of Cartagena, in 2014 and 2019, respectively.

In 2014, he joined the Department of Information Technologies and Communications, UPCT, as a Research Student. In 2016, he began a research project with the objective of developing his Ph.D. thesis, fruit of a collaboration between UPCT and Thales Alenia Space Spain, for the design and development of novel microwave filter structures using additive manufacturing techniques for space applications. In 2020, he joined the Department of Computer Science, Universidad de Alcalá, as a Postdoctoral Researcher in computational electromagnetism. In 2022, he joined the Department of Electrical, Electronical and Communications Engineering, Universidad Pública de Navarra, as a Postdoctoral Researcher, under a Margarita Salas Grant, where he is currently developing his professional activity. His current research interests include the analysis and design of microwave devices employing additive manufacturing and synthesis techniques for the design of microwave filters in various technologies.
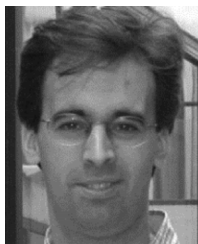
TXEMA LOPETEGI (Member, IEEE) was born in Pamplona, Navarre, Spain, in 1973. He received the M.Sc. and Ph.D. degrees in telecommunication engineering from the Public University of Navarre (UPNA), Pamplona, in 1997 and 2002, respectively. Since 1997, he has been an Assistant Professor with the Electrical, Electronic and Communications Engineering Department, UPNA, where he has been an Associate Professor, since 2006. From 2002 to 2003, he was a Research Fellow with the Payload Systems Division, European Space Research and Technology Centre (ESTEC), European Space Agency (ESA), Noordwijk, The Netherlands. He is the Co-Founder of TAFCO Metawireless S.L., a spin-off company of UPNA. His research interests include metamaterials and synthesized structures in microwave, millimeter-wave, and terahertz (THz) technologies; filters and passive components; and coupled-mode theory and synthesis techniques using inverse scattering and their applications in wireless and space communications. He received a grant from the Spanish Ministry of Education, in 1999 and 2000, to support the research in his doctoral thesis, several prizes, including the Spanish National Prize to the Best Doctoral Dissertations in Telecommunications, in 2003, awarded by COIT/AEIT; and the Extraordinary Doctorate Prize of UPNA.

PETRONILO MARTIN-IGLESIAS (Senior Member, IEEE) was born in Cáceres, Spain, in 1980. He received the Telecommunication Engineering degree from the Polytechnic University of Madrid, Madrid, Spain, in 2002, and the master's degree from the University of Leeds, Leeds, U.K., in 2012.

He has been with industry for over ten years as a Microwave Engineer involved in active (high-power amplifiers for radar applications) and passive (filters, multiplexers, and couplers) RF hardware design, including two years as a Radar System Engineer with Indra Sistemas, Madrid; ISDEFE S.A., Madrid; and Thales Alenia Space Spain, Madrid. Since 2012, he has been with the European Space Agency, Noordwijk, The Netherlands, where he is involved in the research and development and project support activities related to RF passive hardware developments. His current research interests include filter synthesis theory, electromagnetic (EM) design, high-power prediction, and advanced manufacturing techniques for RF passive hardware.

Mr. Martin-Iglesias has been serving as a member for the IEEE Microwave Theory and Techniques Society (IEEE MTT-S) Technical Program Committee (TPC), since 2013.

• • •